# Fisher Information-Based Evaluation of Image Quality for Time-of-Flight PET

Kathleen Vunckx, *Member, IEEE,*, Lin Zhou, *Student Member, IEEE*, Samuel Matej, *Senior Member, IEEE*,
Michel Defrise, *Senior Member, IEEE* and Johan Nuyts, *Member, IEEE*

***Abstract*—The use of time-of-flight (TOF) information during positron emission tomography (PET) reconstruction has been found to improve the image quality. In this work we quantified this improvement using two existing methods: (1) a very simple analytical expression only valid for a central point in a large uniform disk source, and (2) efficient analytical approximations for post-filtered maximum likelihood expectation maximization (MLEM) reconstruction with a fixed target resolution, predicting the image quality in a pixel or in a small region of interest based on the Fisher information matrix. Using this latter method the weighting function for filtered backprojection reconstruction of TOF PET data proposed by C. Watson can be derived. The image quality was investigated at different locations in various software phantoms. Simplified as well as realistic phantoms, measured both with TOF PET systems and with a conventional PET system, were simulated. Since the time resolution of the system is not always accurately known, the effect on the image quality of using an inaccurate kernel during reconstruction was also examined with the Fisher information-based method. First, we confirmed with this method that the variance improvement in the center of a large uniform disk source is proportional to the disk diameter and inversely proportional to the time resolution. Next, image quality improvement was observed in all pixels, but in eccentric and high-count regions the contrast-to-noise ratio (CNR) increased less than in central and low- or medium-count regions. Finally, the CNR was seen to decrease when the time resolution was inaccurately modeled (too narrow or too wide) during reconstruction. Although the maximum CNR is not very sensitive to the time resolution error, using an inaccurate TOF kernel tends to introduce artifacts in the reconstructed image.**

***Index Terms*—FBP, Fisher information, image quality, MLEM, TOF PET.**

## I. INTRODUCTION

In the 1980s considerable research interest emerged for the use of time-of-flight (TOF) information in positron emission tomography (PET). However, due to the lack of fast high efficiency scintillators, this promising route was abandoned until in the 1990s the development of new scintillators, such as lutetium orthosilicate (LSO) and lanthanum bromide ($LaBr_3$), renewed interest in TOF PET. The effect on the image quality of using TOF information during PET reconstruction has been studied extensively by many groups. With analytical calculations [1]–[5], (Monte Carlo) simulations [6]–[13], observer studies [14] and experimental data [9], [15]–[18] it was shown that the image quality improves if timing information is exploited. Many analytical approaches to predict the image quality are, however, restricted to simple objects. And on the other hand, simulations and phantom experiments are very time-consuming or give noisy results due to low-count statistics.

In this work, we use an analytical method, based on approximate expressions for the Fisher information matrix, to predict the impulse response and (co)variance of individual pixels of three phantoms imaged with various 2D TOF PET systems, as well as with a conventional PET system. The Fisher information matrix was used before to study the image quality achievable with 2D TOF PET, but the need for computing its inverse limited the evaluation to small regions of interests or to larger ones with a coarse resolution [19].

During reconstruction, the finite TOF resolution is usually modeled as a Gaussian with a full width at half maximum (FWHM) $\Delta t$, or equivalently $\Delta x = c\Delta t/2$, with $\Delta x$ the localization uncertainty of the TOF PET system, $c$ the speed of light, and $\Delta t$ the time resolution. This Gaussian is often called the TOF kernel. We studied the effect of using an inaccurate width (FWHM) for the TOF kernel, because $\Delta t$ is not always accurately known and might depend on the count rate [16], and because of the counterintuitive results reported in [20], which indicated that using a wider kernel slightly improved the contrast versus noise trade-off.

## II. THEORY

### A. Previous Analytical Calculation of TOF Variance

In 1981, Tomitani derived a formula to evaluate the variance in the center of an infinitely large uniform source, reconstructed with a filtered backprojection (FBP) method using TOF information [2]. He proved that confidence weighted FBP, i.e. weighting the backprojection with the TOF kernel, ensures minimal variance ($\text{Var}_{TOF,min}$)[1], and calculated the variance reduction due to TOF by comparing it to the variance

---

This work was supported in part by F.W.O. grant G.0569.08, in part by 2007 IEEE MIC travel grant, and in part by the National Institutes of Health under grants EB002131 and CA113941.

K. Vunckx, L. Zhou and J. Nuyts are with the Department of Nuclear Medicine, K.U.Leuven, B-3000 Leuven, Belgium (e-mail: kathleen.vunckx@uz.kuleuven.be).

S. Matej is with the Department of Radiology, Univ. of Pennsylvania, Philadelphia, PA 19104 USA.

M. Defrise is with the Department of Nuclear Medicine, V.U.Brussel, B-1090 Brussel, Belgium.

[1] In [2], the reconstructed image represents the total amount of photon pairs detected during acquisition time. Therefore, variance increases with $a$, as in eq. 1. More often, the activity is provided in Bq. Then, variance increases with the activity, but decreases with the scan duration. However, the change in variance due to the use of TOF information is independent of $a$ (see eq. (2)).

obtainable with conventional PET ($\mathrm{Var}_{conv,min}$) in the center of a large (with respect to $\Delta x$) uniform disk phantom with diameter $D$:

$$\mathrm{Var}_{TOF,min} \approx \frac{b^2}{8}\frac{a\Delta x}{\Delta r^3}, \text{ provided that } D >> \Delta x > 2\Delta r \tag{1}$$

and

$$\frac{\mathrm{Var}_{conv,min}}{\mathrm{Var}_{TOF,min}} \approx \frac{b}{2\sqrt{\pi}}\frac{D}{\Delta x} = 0.66\frac{D}{\Delta x} \tag{2}$$

with $b = \sqrt{8\ln 2}$, $a$ the amount of detected coincidences per unit area, and $\Delta r$ the resolution of the reconstructed image, i.e. the resolution of the post-smooth filter since perfect system resolution is assumed. Both $\Delta x$ and $\Delta r$ represent the FWHM.

FBP is very similar to unweighted least squares (LS) reconstruction, assuming that the sampling is sufficiently fine [21]. In weighted least squares (WLS) reconstruction, different sinogram pixels are assigned different weights. However, because of the rotational symmetry of the phantom, the sinogram pixels contributing significantly to the central pixel will all receive nearly the same weight. Consequently, these expressions also hold with good approximation for the central pixel in a WLS reconstruction. It follows that they also apply to maximum a posteriori (MAP) or post-smoothed maximum likelihood expectation maximization (MLEM) in cases where the non-negativity constraint can be ignored, i.e. with sufficiently high counts, because then a Gaussian distribution well approximates the measurement noise.

### *B. Fisher Information-Based Image Quality Prediction*

*1) Basic Equations:* In emission tomography, the local impulse response (LIR) and the covariance image, i.e. the noise correlation between the pixel of interest and the other image pixels, are often used as image quality measures. The LIR and covariance image can be calculated more efficiently by assuming that the reconstruction is locally linear [22], meaning that the mean reconstruction of noisy projection data can be well estimated by the reconstruction of noiseless data. This is valid in case of low noise in the reconstruction image. In [22], [23] efficient analytical approximations for the linearized LIR (LLIR) $l^j$ and the covariance image $\mathrm{Cov}^j$ of a pixel $j$ were proposed for converged MAP reconstruction:

$$l^j(\Lambda) \approx [\boldsymbol{F} + \beta\boldsymbol{U}]^{-1}\boldsymbol{F}e^j \tag{3}$$

$$\mathrm{Cov}^j(\Lambda) \approx [\boldsymbol{F} + \beta\boldsymbol{U}]^{-1}\boldsymbol{F}[\boldsymbol{F} + \beta\boldsymbol{U}]^{-1}e^j \tag{4}$$

$$\text{with } \boldsymbol{F} = \boldsymbol{A^T C_Y^{-1} A} \tag{5}$$

where $\Lambda$ is the unknown activity distribution, $\boldsymbol{F}$ is the Fisher information matrix (which - in emission tomography - can be calculated by a forward projection $\boldsymbol{A}$, weighted by the inverse of the covariance matrix $\boldsymbol{C_Y}$ of the phantom measurement $\boldsymbol{Y}$, and followed by a backprojection $\boldsymbol{A^T}$, with $^{\boldsymbol{T}}$ denoting transpose), $\beta$ is the smoothing parameter, $\boldsymbol{U}$ is the Hessian of the quadratic prior, used for regularization, and $e^j$ is the N×1 unit vector with the $j$-th element equal to one and zero elsewhere, and N the total number of image pixels.

To enable comparison between different systems at equal (uniform) spatial resolution, we adapted the above equations to approximate post-smoothed MLEM with a fixed target resolution [24]. Essentially, $\beta$ was set to 0, and an isotropic Gaussian post-smooth filter $\boldsymbol{P}$ to impose the given target resolution was added. Because $\boldsymbol{F}$ may not be invertible without the regularization of the prior, an approximate pseudoinverse $\boldsymbol{G}$ was introduced (see [24] for the expression for $\boldsymbol{G}$). This yielded the following equations:

$$l^j(\Lambda) \approx \boldsymbol{PGF}e^j \tag{6}$$

$$\mathrm{Cov}^j(\Lambda) \approx \boldsymbol{PGFG^T P^T}e^j. \tag{7}$$

Since we are only interested in local properties of pixel $j$, it is valid to assume that locally the reconstruction problem can be approximated as shift-invariant [23]. Under this assumption, $\boldsymbol{F}$ can be turned into a circulant matrix $\boldsymbol{F^j}$, where each row is a shifted version of the $j$-th row. Accordingly, also $\boldsymbol{G}$ and $\boldsymbol{P}$ become $j$-dependent (and get therefore a superscript $^j$). Equations (3)-(7) can then be calculated by convolutions in the spatial domain, or - more efficiently - by multiplications in the Fourier domain [23]. Consequently, equations (6) and (7) changed into[2]:

$$l^j(\Lambda) \approx \boldsymbol{P^j G^j F^j}e^j \tag{8}$$

$$\mathrm{Cov}^j(\Lambda) \approx \boldsymbol{P^j G^j F^j G^{jT} P^{jT}}e^j. \tag{9}$$

Approximations (3) and (4) have been studied and validated for various systems, including 2D and fully 3D PET [22], [23]. As shown in [25], MAP and post-smoothed MLEM have similar noise performance if the resolution is carefully matched, making equations (6) and (7) equivalent to equations (3) and (4) for matched resolution. In addition, the approximations for post-smoothed MLEM were validated for a more challenging, i.e. more shift-variant application, namely multipinhole SPECT [24]. Therefore, the approximations are expected to be accurate for predicting 2D conventional and TOF PET image quality as well. To justify this statement, a validation study in the most realistic phantom of those considered in this paper was performed (see section III-C).

The $j$-th elements of $l^j(\Lambda)$ and $\mathrm{Cov}^j(\Lambda)$ are the contrast recovery coefficient (CRC), i.e. the value of the LLIR at the location of the impulse, and the variance (Var) in pixel $j$, respectively. Combined they yield the contrast-to-noise ratio (CNR), often used as an image quality measure:

$$\mathrm{CNR} = \frac{\mathrm{CRC}}{\sqrt{\mathrm{Var}}}. \tag{10}$$

Note that an increase in measured activity has a different effect on the (co)variance depending on whether the total amount of emitted photon pairs are reconstructed or the activity in the field of view (i.e., the count rate). Usually one is interested in the activity distribution in the patient (e.g., expressed in Bq or Bq/cc). Then, the (co)variance is proportional to the activity and inversely proportional to the acquisition time. Indeed, the (co)variance is inversely proportional to the Fisher information matrix, which in turn is proportional to the acquisition time

---

[2] If $\boldsymbol{P^j}$ represents a Gaussian filter, $\boldsymbol{P^{jT}}=\boldsymbol{P^j}$ because the same Gaussian filter, which was optimized to ensure the target resolution in pixel $j$, is applied to the whole image. This means that every row $k$ (and therefore also every column $k$) of $\boldsymbol{P^j}$ represents this Gaussian filter centered around pixel $k$, and hence, $\boldsymbol{P^j}$ is a symmetrical matrix.

(see equation (5) with $A \propto T$ and $C_Y \propto T$), and inversely proportional to the activity in the field of view. In this work, we compare PET systems that are identical except for their time-of-flight information. Therefore, the ratio of the variances is insensitive to the measured activity (as was the case in equation (2)).

*2) Extension to Regions of Interest:* Assuming local shift-invariance, the filters found for an individual pixel $j$ (see equations (8) and (9)) should be good approximations for all pixels of a small region of interest (ROI) centered at $j$. Therefore, the post-smoothed LLIR ($l^{ROI}$), the mean in the ROI (Mean$^{ROI}$) and the variance on this mean (Var$^{ROI}$) can be approximated as

$$l^{ROI}(\Lambda) \approx Q_I R \tag{11}$$

$$\text{Mean}^{ROI}(\Lambda) \approx \frac{1}{r} R^T Q_I R \tag{12}$$

$$\text{Var}^{ROI}(\Lambda) \approx \frac{1}{r^2} R^T Q_V R \tag{13}$$

with $Q_I = \boldsymbol{P}^j \boldsymbol{G}^j \boldsymbol{F}^j$ and $Q_V = \boldsymbol{P}^j \boldsymbol{G}^j \boldsymbol{F}^j \boldsymbol{G}^{jT} \boldsymbol{P}^j$, which can be obtained from equations (8) and (9), with $R$ an N×1 vector in which all elements indicating a pixel inside the ROI equal one and all others equal zero, and with $r$ the number of pixels in the ROI.

*3) Extension to Mismatched TOF Kernels:* Equations (8) and (9) can easily be extended to predict the impulse response and covariance image of pixel $j$ reconstructed with a mismatched TOF kernel. The derivations can be found in Appendix A and yield the following approximations:

$$l^j(\Lambda) \approx \boldsymbol{P}^j \boldsymbol{G}^j_{BB} \boldsymbol{F}^j_{BA} e^j \tag{14}$$

$$\text{Cov}^j(\Lambda) \approx \boldsymbol{P}^j \boldsymbol{G}^j_{BB} \boldsymbol{F}^j_{BB} \boldsymbol{G}^{jT}_{BB} \boldsymbol{P}^j e^j \tag{15}$$

with $\boldsymbol{G}^j_{BB}$, $\boldsymbol{F}^j_{BA}$ and $\boldsymbol{F}^j_{BB}$ the shift-invariant versions of $\boldsymbol{G}_{BB}$ ($= [\boldsymbol{B}^T \boldsymbol{C_Y}^{-1} \boldsymbol{B}]^{ps}$), $\boldsymbol{F}_{BA}$ ($=\boldsymbol{B}^T \boldsymbol{C_Y}^{-1} \boldsymbol{A}$) and $\boldsymbol{F}_{BB}$ ($=\boldsymbol{B}^T \boldsymbol{C_Y}^{-1} \boldsymbol{B}$), respectively. $\boldsymbol{B}$ and $\boldsymbol{B^T}$ are defined similarly to $\boldsymbol{A}$ and $\boldsymbol{A^T}$ as the forward and backward projection matrix modeling the reconstruction TOF kernel with inaccurate time resolution. $^{ps}$ represents approximate pseudoinverse. Careful use of these approximations is recommended, as they become inaccurate and unstable for very eccentric pixels and reconstruction kernels that are much wider than the real ones.

### C. Fisher Information-Based Backprojection Weighting Function Derivation for FBP of TOF PET

The above Fisher information-based approximations can also be used to determine the weighting function for FBP reconstruction yielding minimal variance in the central point of a rotationally symmetrical positron emitting object, imaged with a TOF PET system. This weighting function was derived earlier in [26] in a heuristic way, and was found to be $\sigma^2 = \sigma^2_{TOF}(1 + \sigma^2_{TOF}/\sigma^2_{obj})$. The derivation of this weighting function using the Fisher information-based method is presented in Appendix B.

## III. SIMULATIONS

### A. Homogeneous Disk, no Attenuation

For the first experiment, two homogeneous disk phantoms with a diameter of 20 cm and 35 cm were simulated in order to mimic a 2D slice of a slim and a heavy patient, respectively. We examined the reconstruction image quality in the central pixel, obtainable with 12 different idealized 2D TOF PET tomographs with a time resolution $\Delta t$ ranging from 100 to 1500 ps FWHM, and with a conventional PET system. For each system, the variance in this pixel was calculated twice: first from the approximation derived by Tomitani (equation (2)) and second from the Fisher information-based approximation (equation (9)).

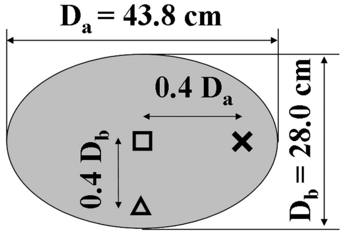

Fig. 1. Illustration of the dimensions of the water-filled ellipse and the location of the investigated points.

The simulations produced sinograms of size 336x336(x84) (detector pixels x projection angles (x time bins[3])) for (TOF) PET, with a spatial and time sampling of 0.2 cm and 53.3 ps, respectively. The image space consisted of 336x336 square pixels of 0.2 cm. Post-smoothing ensured a resolution of 0.6 cm FWHM. Attenuation, scatter, randoms and detector resolution were not modeled.

### B. Homogeneous Ellipse

Since 2D transaxial slices of a patient are usually more ellipse-shaped and attenuation is not negligible, a water-filled ($\mu = 0.096\ \text{cm}^{-1}$) elliptical phantom with the same area as the 35 cm diameter disk phantom was simulated. The long axis-to-short axis diameter ratio ($D_a/D_b$) was taken 1.56, which results in a $D_a$ and $D_b$ of 43.8 cm and 28.0 cm, respectively. Using equation (9), the variance was examined in three points: the central pixel and two pixels located along the two axis of the ellipse at a distance of 80% of $D_a/2$ and $D_b/2$ from the center, respectively (see Fig. 1).

The same TOF and non-TOF PET systems were simulated as for the previous phantom. Also the image parameters were left unchanged. Attenuation was modeled, but scatter, randoms and detector resolution were not considered in the simulation.

### C. Realistic 2D Thorax Phantom

To get a feeling of the gain that can be expected from imaging a real patient with a TOF PET system, a 2D thorax phantom with realistic activity distribution and attenuation values was simulated (see Fig. 2(a)). Although TOF PET is known to reduce the effect of randoms on the image quality [27], the inclusion of randoms in the model was considered out of the scope of this work. The actual gain

---

[3] For all simulations the time bins were equally distributed over the complete field of view, which was defined by the number of detector pixels. The time bin spacing was thus constant for TOF PET systems with different time resolutions (within the same simulation study).

Fig. 2. Illustration (a) of the realistic 2D thorax phantom (activity distribution), and of a post-smoothed reconstruction image from (b) simulated conventional PET data and (c) simulated TOF PET data with a time resolution of 500 ps FWHM.

due to the use of TOF information during reconstruction will therefore be underestimated. Scatter was ignored as well.

The phantom was obtained by thresholding the CT image of a clinical FDG PET/CT scan of a patient with several tumors in the lungs. The mean linear attenuation coefficient was calculated in each region and scaled to fit typical values at 511 keV to build the attenuation map. Next, these regions were assigned a realistic uptake value, based on the corresponding values in the real PET image (see Fig. 2(a)). The simulated PET represents a 20 minutes 2D acquisition of a patient injected with 200 MBq FDG, which should provide similar statistical information as a 4 min scan in 3D mode.

The image quality of the thorax phantom was evaluated for two systems, i.e. a TOF PET system with a time resolution of 500 ps FWHM and a conventional PET system. The variance image for either PET system was obtained in two different manners. First, the variance was calculated in each pixel using equation (9). Next, the variance image was derived from the post-smoothed MLEM reconstruction of 300 projection data sets of the phantom corrupted with semi-random Poisson noise. Fig. 2(b) and (c) show an example non-TOF and TOF PET reconstruction image. The MLEM reconstructions were accelerated using ordered subsets [28]. OSEM was used to accelerate convergence, and the number of subsets was gradually reduced to ensure convergence to the maximum likelihood solution. The used iteration scheme was 15×32, 10×16, 5×8, 5×4, 3×2, 3×1 (global iterations × number of subsets), corresponding to 709 sub-iterations (updates). Dividing the variance image of the non-TOF by that of the TOF PET system will show the variance improvement (also called gain in the rest of the paper) throughout the phantom.

The intrinsic resolution of the detector was taken 0.5 cm FWHM. The sinograms were of size 192×192(×96) for (TOF) PET, with a radial sampling of 0.3375 cm. The TOF data were sorted in 96 time bins of 45 ps to cover the whole FOV (4.32 ns, or equivalently 64.8 cm). As mentioned above, no scatter nor randoms were modeled. The mean total counts in the sinograms was about $10^6$ counts. This corresponds to a mean of 28 counts per detector pixel (max. 198) for conventional PET and 0.3 counts per time bin (max. 12) for TOF PET. The image space had 192×192 square pixels of 0.3375 cm. The target resolution was 1.2 cm FWHM.

Compared to the simulation with the homogeneous ellipse, the pixel size was increased from 0.2 cm to 0.3375 cm to speed-up the calculation of the variance images. Correspondingly, the target resolution was increased, because a minimal amount of post-smoothing is required for stability and accuracy of the approximations.

### D. Effect of TOF Kernel Accuracy

As a last simulation study, the effect on the image quality of modeling the time resolution with an inaccurate kernel during reconstruction is investigated. Because we want to compare the results of our study (obtained with the Fisher information-based method) to those presented in [20] (based on the reconstruction of noisy projection data sets), the simulation parameters were taken as similar as possible, and the image quality in a ROI rather than in a pixel was investigated. Since in this work the contrast is directly obtained from the impulse response, a homogeneous disk phantom of 27 cm diameter is simulated instead of a hot-spheres phantom of the same size. The mean and the variance on the mean in a 1.3 cm diameter ROI at 7 cm from the center can then be calculated from equations (12) and (13). Dividing the mean value by the square root of the variance yields the CNR.

The time resolution of the simulated TOF PET scanner was modeled as a Gaussian with a FWHM of 300 ps. The image quality obtained with a variety of reconstruction TOF kernel resolutions, i.e. 150, 225, 300, 375, 450, and 600 ps FWHM, was evaluated using a combination of equations (11)-(13) and equations (14)-(15). The attenuation of water was modeled, but scatter, randoms and detector resolution were not considered. The dimensions of the sinogram and of the image space were 336x336x48 and 336x336, respectively. The spatial sampling was 0.2 cm, the time sampling was 93.3 ps, and the pixel size was taken 0.2x0.2 $\mathrm{cm}^2$. A target resolution of 0.6 cm FWHM was imposed.

To investigate the influence of a mismatched TOF kernel on the quantitation accuracy, three images of the same noiseless projection data set were reconstructed. The measurement of the homogeneous disk phantom, described above, with a TOF PET system with a time resolution of 300 ps FWHM was simulated. The activity in the eccentric ROI was doubled compared to the background activity. The post-smoothed OSEM reconstructions were run with 709 updates (equivalent to 709 MLEM iterations) and TOF kernels with a FWHM of 150, 300 and 600 ps were used to obtain the three reconstruction images.

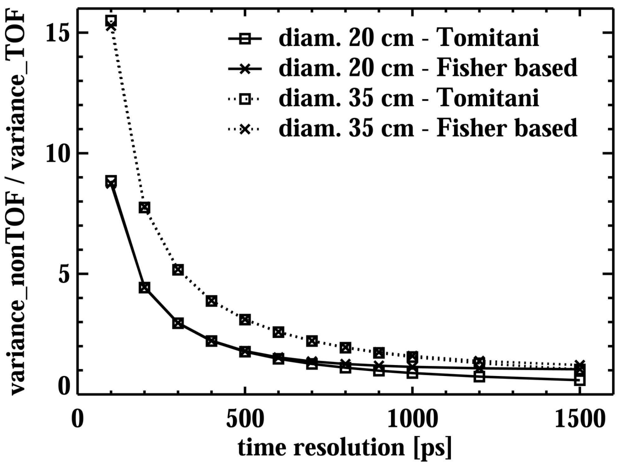

Fig. 3. Simulation 1: Variance improvement due to the use of TOF information plotted versus the time resolution of the TOF PET systems. The image quality of the central pixel of two uniform disk phantoms with a diameter of 20 (solid lines) and 35 cm (dotted lines), respectively, was investigated with two methods: (squares) Tomitani's method (equation (2)), and (crosses) the Fisher information-based method (equation (9)).

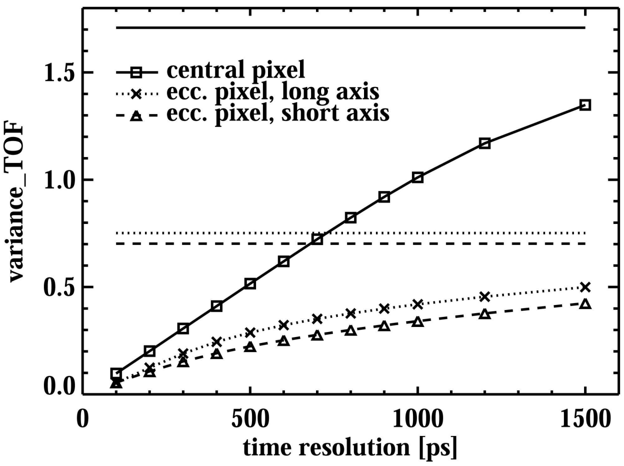

Fig. 4. Simulation 2: Variance in 3 points of a homogeneous water-filled ellipse is plotted with respect to the time resolution of the tested systems. The horizontal lines show the results for the conventional PET system. The long and short axis diameter is 43.8 cm and 28.0 cm, respectively. The central pixel (squares, solid lines), the eccentric pixel on the long axis (crosses, dotted lines) and on the short axis (triangles, dashed lines) were investigated.

## IV. RESULTS

### A. Homogeneous Disk, no Attenuation

In Fig. 3, the variance improvement in the central pixel of both the 20 cm (solid lines) and the 35 cm (dotted lines) diameter uniform disk source obtained due to the use of TOF information is plotted with respect to the time resolution $\Delta t$ of the TOF PET systems. Two prediction methods are compared: (1) Tomitani's approximation (results depicted with squares) and (2) the Fisher information-based method (results plotted as crosses). The predictions of the two methods closely match, especially for good time resolutions and for a large diameter. The approximation of Tomitani incorrectly predicts that for smaller phantoms the image quality is better using a conventional PET system than using a TOF PET system with bad time resolution. This is because the assumption $D >> \Delta x$ that was made to derive equation (2) is no longer valid.

### B. Homogeneous Ellipse

Fig. 4 plots the variance for the three pixels in the water-filled ellipse (see Fig. 1) versus the time resolution of the TOF PET systems. The horizontal lines depict the variance obtained with the conventional PET system. For all PET systems the variance in the central pixel (squares, solid lines) is clearly higher than the variance in the eccentric pixels (crosses, dotted lines and triangles, dashed lines). The variance in the eccentric pixel on the short axis (triangles, dashed lines) is slightly lower than that on the long axis (crosses, dotted line).

The evolution of the improvement in variance in the three points is denoted in table I. The gain was shown for first generation, current generation and future generation TOF PET systems with a time resolution of 1500, 500 and 100 ps, respectively. The eccentric pixels start to benefit from the TOF information already at modest time resolutions (factors 1.50 and 1.65 for eccentric points vs. a factor 1.27 for the central one at $\Delta t$ =1500 ps), but the variance decreases faster with improved time resolution in the central pixel (gain close to 18 for the central pixel vs. 13-14 for the eccentric ones).

TABLE I
VARIANCE IMPROVEMENT IN THREE POINTS OF A WATER-FILLED ELLIPSE.

| $\Delta t$ | 100 ps | 500 ps | 1500 ps |
|---|---|---|---|
| Central point | 17.58 | 3.31 | 1.27 |
| Point at $0.4D_a$ | 13.92 | 2.61 | 1.50 |
| Point at $0.4D_b$ | 12.75 | 3.13 | 1.65 |

### C. Realistic 2D Thorax Phantom

The calculated variance and gain images of the thorax phantom with modeled attenuation (see Fig. 2(a)) are shown in Fig. 5. The left column contains the variance and gain images predicted with the Fisher information-based method, in the central column the corresponding images obtained from the reconstruction of 300 noisy projection data sets are shown. The variance images expected from the TOF PET system with $\Delta t = 500$ ps FWHM are shown on the first row. The variance images predicted for the conventional PET system can be seen on the middle row. The last row illustrates the distribution of the variance improvement over the thorax phantom, calculated with both methods. To facilitate comparison, the absolute difference images are presented in the last column, using the same scale as the variance/gain images, respectively.

From the first two rows in Fig. 5 it is clear that the variance reduces when TOF information is available during reconstruction. As $\Delta t$ decreases, the variance images become similar to the thorax image (see Fig. 2(a)), because imaging with excellent time resolution results in an image of the phantom corrupted by Poisson noise. Hence, the Fisher information-based method will simply predict the variance on the phantom activity distribution when it is post-smoothed to ensure the target resolution. From the gain images (see Fig. 5E and F),

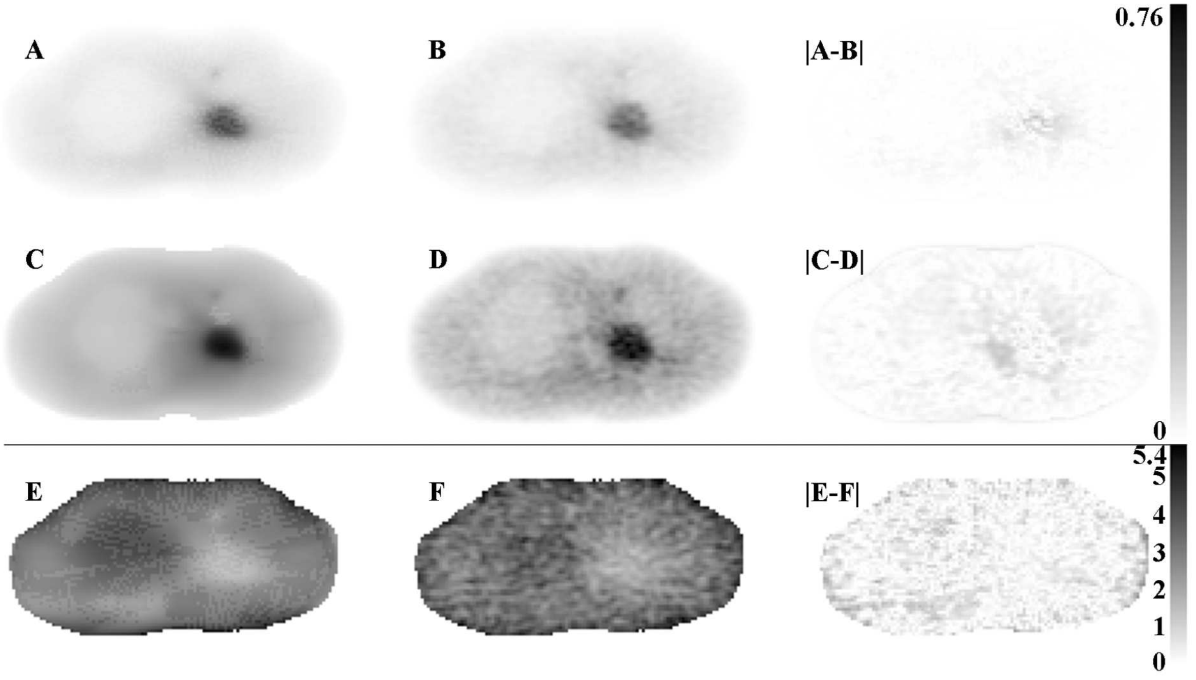

Fig. 5. Simulation 3: Evaluation of the effect of the use of TOF PET for a realistic 2D thorax phantom. Variance images expected for a TOF PET system with a time resolution of 500 ps FWHM (top row) and for a conventional PET system (middle row) were obtained with the Fisher information-based method (first column) as well as with the reconstruction of 300 noisy projection data sets (second column). From these variance images the corresponding distribution of the variance improvement was calculated (bottom row). In the last column, the absolute difference images are shown using the same scale as the original images.

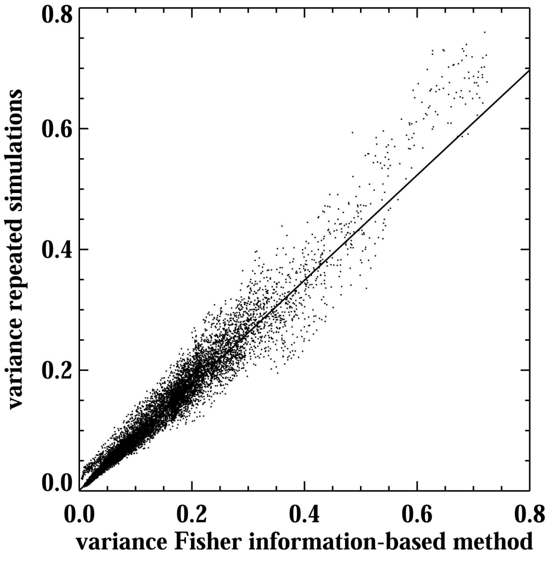

Fig. 6. Simulation 3: Validation of the Fisher information-based variance calculation method. For all pixels inside the thorax phantom, the variance obtained with 300 repeated simulations is plotted with respect to the variance predicted with the Fisher information-based method. The results for both TOF (Fig. 5A and B) and conventional PET (Fig. 5C and D) are included. The solid line represents the weighted least squares fit through the data.

we can conclude that the variance reduction is minor in the high count regions and up to a factor 4-5 in the large low active lung. The absolute difference images show that the predictive value of the approximate method is very good. The nice correlation between the variances calculated with two different methods could also be seen when plotting the reconstruction-based variance with respect to the estimated variance (see Fig. 6). The square of the correlation coefficient equals 0.95. A weighted least squares fit resulted in a line with slope 0.87 and intercept 0.001.

### D. *Effect of TOF Kernel Accuracy*

In Fig. 7, the mean (left), the variance on the mean (center) and the CNR of the ROI (right) are plotted with respect to the FWHM of the reconstruction TOF kernel. The top row shows the results for the standard case, where $\boldsymbol{P}^j$ was the Gaussian post-smooth filter that imposes the 6 mm FWHM target resolution. As can be seen, both the mean and the variance increase with increasing kernel width. When the kernel was taken too narrow ($<$ 300 ps), the mean decreased faster than the variance. On the contrary, when the kernel was taken too wide ($>$ 300 ps), the mean increased slower than the variance. As a result, the best contrast versus variance trade-off was obtained using the correct kernel (300 ps FWHM).

One should note, however, that - due to the fixed target resolution - the mean value in the ROI was expected to be constant. The fact that it is not, can be explained by investigating the shape of the post-smoothed impulse response. For the narrowest and widest kernel, profiles of these are drawn as a dashed line in the left and right top graph of Fig. 8, respectively. These impulse responses, post-smoothed with the target Gaussian filter (6 mm FWHM) are compared to the ideal ROI smoothed with this target Gaussian (solid curve). From the top images a clear under- and overshoot can

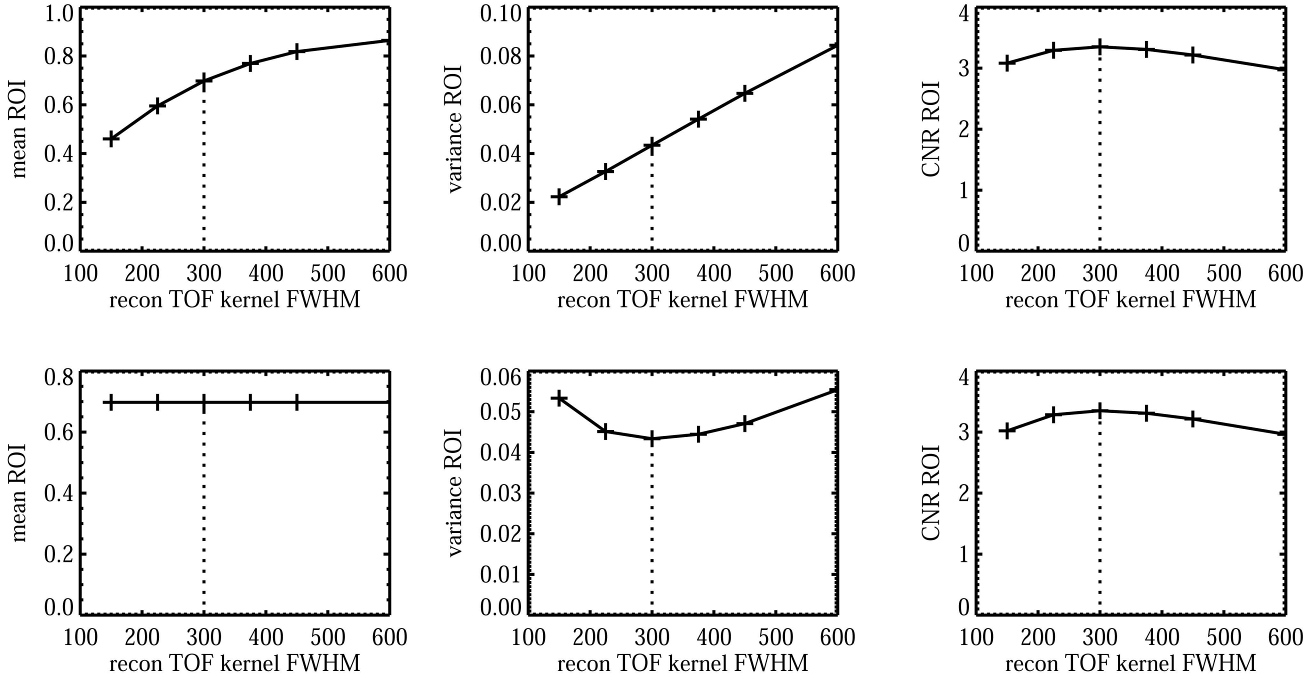

Fig. 7. Simulation 4: Mean, variance on the mean, and CNR of the eccentric ROI in the 27 cm diameter homogeneous sphere (described in section III-D) plotted with respect to the TOF kernel used during reconstruction. The real TOF kernel had a resolution of 300 ps. Top: Gaussian post-filter. Bottom: optimal post-filter.

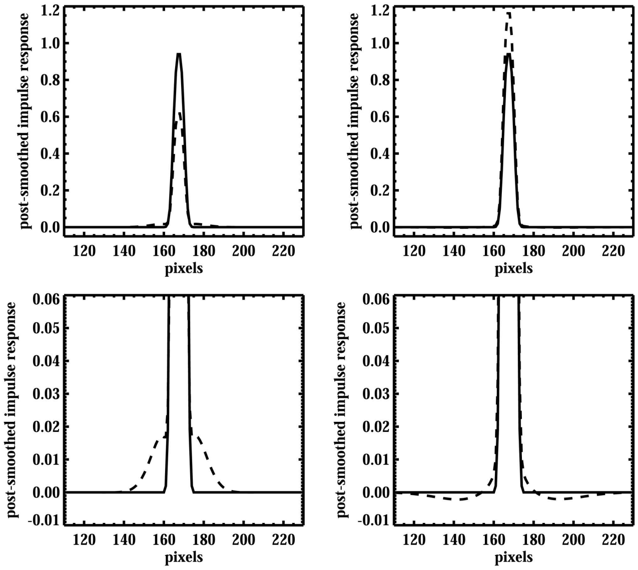

Fig. 8. Simulation 4: Illustration of the artifacts in the post-smoothed impulse response caused by using an inaccurate TOF kernel during reconstruction. The solid lines show the ideal ROI post-smoothed with a Gaussian with a FWHM of 6 mm (target resolution). The dashed lines plot the post-smoothed impulse response obtained with a too narrow kernel (left) and a too wide kernel (right), respectively. Top row: full range. Bottom row: zoomed-in on the bottom part of the impulse response.

be observed for the narrow and wide kernel, respectively. Correspondingly, sidelobes and undershoots outside the FWHM range are observed in the bottom row images, which are a zoomed-in version of the top ones.

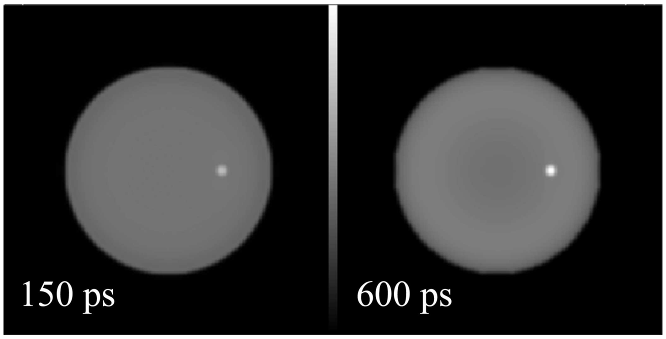

Fig. 9. Homogeneous 27 cm diameter disk with an impulse in a 1.3 cm diameter ROI at 7 cm from the center, after reconstruction with a TOF kernel with a FWHM of (left) 150 ps, (right) 600 ps. The real TOF kernel was 300 ps.

The same effects are visible in Fig. 9 and Fig. 10. Fig. 9 shows two of the reconstruction images of the homogeneous phantom with an eccentric ROI containing twice the amount of background activity. The left image was obtained using a too narrow reconstruction TOF kernel (150 instead of 300 ps FWHM). Using a too wide TOF kernel (600 ps FWHM) during reconstruction, yielded the right image. In Fig. 10, the vertical and horizontal profiles through the center of the ROI are plotted for the too narrow (dotted line), correct (solid line) and too wide (dashed line) TOF kernel. Similar under- and overshoots as found in Fig. 8 can be recognized.

Because it is more intuitive to compare the image quality at equal contrast, the post-filtering $\boldsymbol{P}^j$ had to be adapted such that it ensures that not only the width but also the shape

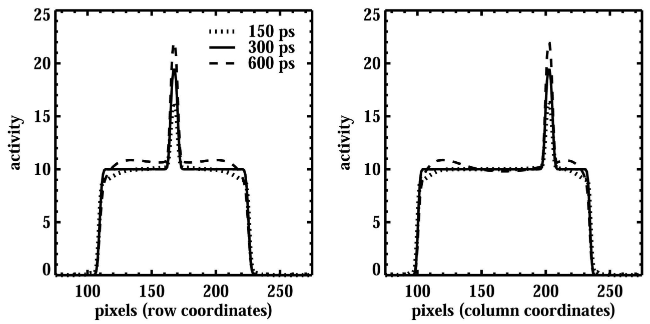

Fig. 10. The vertical (left) and horizontal profiles (right) through the center of the ROI of the reconstructed images of Fig. 9 are plotted as a dotted line (150 ps), solid line (300 ps) and dashed line (600 ps).

of the post-filtered impulse response agrees with the target Gaussian filter. This new $\boldsymbol{P}^j$ is calculated in the Fourier domain by dividing the fast Fourier transform (FFT) of the target Gaussian filter by the FFT of the unfiltered LLIR. The results obtained with this optimal post-filter are shown on the bottom row of Fig. 7. Again the mean, the variance and the CNR of the ROI were plotted versus the reconstruction TOF kernel. Obviously, the mean of the ROI is now fixed and equal to the value obtained with the 300 ps FWHM reconstruction kernel and Gaussian post-smoothing (see top left graph of the same figure). All effects of the reconstruction kernel accuracy are now contained by the variance, or equivalently, by the CNR. An almost identical CNR curve, with the same optimum, was found using the optimal post-filter instead of the Gaussian post-smooth filter.

## V. DISCUSSION

Tomitani's approximations (1) and (2) were most accurate for central pixels in objects that are much larger than the time resolution. This observation was expected, because these approximations were derived for the center of an infinitely large homogeneous disk source.

The TOF information can rule out a large fraction of the random coincidences, as most of them are detected in distinct time bins. Therefore, TOF PET will probably induce larger variance reduction compared to conventional PET than predicted by Tomitani's formula or by the method presented in this work. The effect of randoms on the image quality of TOF PET was discussed in [27] based on FBP reconstructed experimental data, and an extended version of equation (2) including the influence of randoms was proposed[4]. As in [2], these equations are only valid to predict the image quality of the central pixel of a large homogeneous disk or cylindrical phantom, and therefore are not representative for the gain in variance in an MLEM reconstruction of a patient measurement. In principle, the Fisher information-based method can predict the local properties of any pixel in any phantom. If models for randoms, scatter, etc. are available, they can be included in the calculation of the Fisher information matrix to study their effect on the image quality (although this is beyond the scope of this paper). It is, however, restricted to low noise data, because the non-negativity constraint is not incorporated. This makes the method less appropriate for estimating the gain in real patient data. The method is also readily extensible to 3D TOF PET, where its benefit compared to repeated reconstructions will increase, because the latter become very time-consuming.

The efficiency of the Fisher information-based method allows rapid evaluation of the effect of different parameters (such as the object shape, the attenuation, the time resolution, etc.) on the reconstruction image quality of a few individual pixels or ROIs. To obtain complete variance images faster methods are available [29], but were not used for the calculations presented in this paper.

In [30] some results were slightly different from those presented in this article. The differences in the outcome of the Fisher information-based method are mainly due to more accurately modeling the Gaussians of the TOF kernels and of the post-smooth filters. The tails of the Gaussians were only cut-off at three instead of two standard deviations distance from the mean. In both cases, the values were normalized such that the total equals one, resulting in a decreased maximum value of the Gaussian. Thanks to this more accurate modeling, the curves in Fig. 3 better match those obtained with Tomitani's approximation.

Also the variance images of the thorax were slightly different in [30], especially the one based on reconstructions of noisy non-TOF PET data (see Fig. 5D, underestimation of the variance in the lung in [30]). In this paper the reconstructions were run for an equivalent of 709 MLEM iterations instead of 214 in [30], because the reconstructions were not yet converged. Since the reconstruction of non-TOF PET data converges slower than that of TOF PET data, this change had more effect on Fig. 5D than on Fig. 5B. As the approximate method predicts the variance of MLEM post-smoothed after convergence, the agreement between the analytically calculated variance images and those based on reconstructions improved. The variance images predicted with the Fisher information-based method (Fig. 5A and C) are smooth because neighboring pixels suffer from similar amounts of noise. In contrast, the variance images obtained from the reconstruction of repeated measurements are rather noisy due to the limited number of different noise realizations. Similarly, the variance improvement image obtained with the analytical method is more smooth than that based on reconstructions, which is the result of a division of two noisy images. Fig. 5|E-F| shows that the gain can be predicted well all over the phantom.

In Fig. 5E and F the variance in the tumor is seen to decrease less than the variance in the rest of the thorax. This might possibly be explained as follows. TOF PET reduces the crosstalk between neighboring tissues. In the tumor this crosstalk was already low, hence the benefit is expected to be lower than in other tissues. Furthermore, the lung at the left side of the image gains more than the lung at the right side. Indeed, the former is positioned much farther from the hot tumors than the latter, which might be the reason why it already benefits at 500 ps time resolution.

The top left graph of Fig. 7 is in agreement with the findings in [20]. However, from the same experiment we

---

[4] We believe that the scaling factor $\sqrt{0.66}$ was accidently omitted in [27].

could also conclude that the CNR is optimal when using the correct kernel during reconstruction, whereas in [20] the increased contrast seemed to overcompensate the increase in noise. The main differences between the two methods are the way the figure-of-merit (FOM) for the noise is calculated and the reconstruction method. In [20] the noise was determined from the pixel-to-pixel percent standard deviation (%SD) in background ROIs, averaged over 60 background ROIs. However, due to the rather shift-variant character of the image quality, the variation in background ROIs is not necessarily a good estimator for the variation in the ROI under investigation. The variance (or standard deviation) on the mean value of the ROI is considered to be a more accurate and more representative noise FOM. In [20] the image quality was evaluated after different numbers of iterations, but no matched resolution was assured, which makes it very difficult to fairly compare image quality. Also convergence speed might differ for different TOF kernels. In this work, we have post-smoothed the MLEM reconstructions, run until convergence, to overcome these difficulties.

The CNR curves in the right column of Fig. 7 indicate that small deviations from the real kernel, or equivalently from the effective time resolution, only have a minor effect on the image quality as measured by the CNR. However, these kernel inaccuracies also induce over- or underestimation of the ROI values (in combination with low amplitude sidelobes (see Fig. 8), which compromises the quantitative accuracy, as shown in Fig. 9 and Fig. 10. Fortunately this image degradation is rather limited. Results for significant kernel mismatches were shown to enable clear illustration of the effects.

We can also conclude that the image degrading effects due to the use of a too narrow kernel are much more localized than the ones caused by a too wide kernel. A too narrow rather than a too wide choice of the kernel width is therefore preferable. This effect and its cause are very similar to what is observed when a reconstruction algorithm incorporates a model of the finite resolution of the detectors, that either under- or overestimates the width of the corresponding detector point spread function [31]. In [32] similar artifacts were observed after reconstruction of simulated TOF PET data with mismatched TOF kernels. The importance of these artifacts in reconstruction images of measured data is still to be verified.

## VI. CONCLUSION

Analytical Fisher information-based approximations were used to evaluate the image quality of simple and more realistic phantoms imaged with 2D (TOF) PET systems. The linearized local impulse response, the covariance matrix and the contrast-to-noise ratio in individual pixels and small regions of interest were calculated to compare TOF PET systems with different time resolutions with each other and with a conventional PET system. The approximations were validated with the post-filtered MLEM reconstruction of hundreds of noisy projection data sets. TOF information was found to improve the image quality in all pixels, although less benefit was seen in eccentric and hot regions, since they already performed well in conventional PET. Using a too narrow or too wide TOF kernel for reconstruction tends to decrease the image quality and to cause artifacts in the reconstructed image.

## APPENDIX A
## DERIVATION OF APPROXIMATIONS FOR MISMATCHED TOF KERNELS

We can easily include the reconstruction TOF kernel in equations (6) and (7). First, we insert equation (5) in these equations to obtain

$$l^j(\Lambda) \approx \boldsymbol{P}^j[\boldsymbol{A}^T\boldsymbol{C}_{\boldsymbol{Y}}^{-1}\boldsymbol{A}]^{ps}\boldsymbol{A}^T\boldsymbol{C}_{\boldsymbol{Y}}^{-1}\boldsymbol{A}e^j \qquad \text{(A-1)}$$

$$\text{Cov}^j(\Lambda) \approx \boldsymbol{P}^j[\boldsymbol{A}^T\boldsymbol{C}_{\boldsymbol{Y}}^{-1}\boldsymbol{A}]^{ps}\boldsymbol{A}^T\boldsymbol{C}_{\boldsymbol{Y}}^{-1}\boldsymbol{A} \\ ([\boldsymbol{A}^T\boldsymbol{C}_{\boldsymbol{Y}}^{-1}\boldsymbol{A}]^{ps})^T\boldsymbol{P}^j e^j \qquad \text{(A-2)}$$

where ${}^{ps}$ denotes approximate pseudoinverse, and $\boldsymbol{A}$ denotes projection with the correct TOF kernel (i.e. in agreement with the measurement). We define $\boldsymbol{B}$ as the projection operator using the mismatched TOF kernel.

Next, we identify which projection and backprojection operations need to model the real measurements, and which the reconstruction. For the latter, $\boldsymbol{A}$ and $\boldsymbol{A}^{\boldsymbol{T}}$ are substituted by $\boldsymbol{B}$ and $\boldsymbol{B}^{\boldsymbol{T}}$, respectively. This turns equations (A-1) and (A-2) into

$$l^j(\Lambda) \approx \boldsymbol{P}[\boldsymbol{B}^T\boldsymbol{C}_{\boldsymbol{Y}}^{-1}\boldsymbol{B}]^{ps}\boldsymbol{B}^T\boldsymbol{C}_{\boldsymbol{Y}}^{-1}\boldsymbol{A}e^j \qquad \text{(A-3)}$$

$$= \boldsymbol{P}\boldsymbol{G}_{BB}\boldsymbol{F}_{BA}e^j \qquad \text{(A-4)}$$

$$\text{Cov}^j(\Lambda) \approx \boldsymbol{P}[\boldsymbol{B}^T\boldsymbol{C}_{\boldsymbol{Y}}^{-1}\boldsymbol{B}]^{ps}\boldsymbol{B}^T\boldsymbol{C}_{\boldsymbol{Y}}^{-1}\boldsymbol{B} \\ ([\boldsymbol{B}^T\boldsymbol{C}_{\boldsymbol{Y}}^{-1}\boldsymbol{B}]^{ps})^T\boldsymbol{P}e^j \qquad \text{(A-5)}$$

$$= \boldsymbol{P}\boldsymbol{G}_{BB}\boldsymbol{F}_{BB}\boldsymbol{G}_{BB}^T\boldsymbol{P}e^j \qquad \text{(A-6)}$$

where $\boldsymbol{A}e^j$ represents the impulse measurement (modeled by the correct kernel), and $\boldsymbol{B}^T\boldsymbol{C}_{\boldsymbol{Y}}{}^{-1}$ and $[\boldsymbol{B}^T\boldsymbol{C}_{\boldsymbol{Y}}{}^{-1}\boldsymbol{B}]^{ps}$ can be seen as the (weighted) backprojection and the reconstruction filter (using the inaccurate kernel model), respectively, similar to FBP reconstruction (see Appendix B). $\boldsymbol{P}$ is again the post-smooth filter. The covariance matrix $\text{Cov}^j(\Lambda)$ is computed by propagating the Poisson noise on the data through the reconstruction operator using a quadratic approximation, i.e. a second order Taylor approximation. Because the reconstruction operator uses the inaccurate TOF kernel, the covariance matrix is a function of $\boldsymbol{B}$ and not of $\boldsymbol{A}$.

As before, local shift-invariance is assumed to simplify the calculations: $\boldsymbol{F}_{XX}$ is approximated by the circulant matrix $\boldsymbol{F}^j_{XX}$, yielding equations (14) and (15). The pseudoinverse is again calculated in the Fourier domain and approximated as proposed in [24] as:

$$\mathbf{G}^j_{BB} = \frac{\mathbf{F}^{j*}_{BB}\max\left(\Re(\mathbf{F}^j_{BB}), 0\right)}{\mathbf{F}^{j*}_{BB}\mathbf{F}^j_{BB}\max\left(\Re(\mathbf{F}^j_{BB}), 0\right) + \epsilon} \qquad \text{(A-7)}$$

with $\mathbf{G}^j_{BB}$ and $\mathbf{F}^j_{BB}$ the Fourier transform of $\boldsymbol{G}^j_{BB}$ and $\boldsymbol{F}^j_{BB}$, respectively, ${}^*$ the complex conjugate, $\Re(\mathbf{F}^j_{BB})$ the real part of $\mathbf{F}^j_{BB}$ and $\epsilon = 10^{-10}|\mathbf{F}^j_{BB,DC}|^3$, where $\mathbf{F}^j_{BB,DC}$ denotes the DC value of $\mathbf{F}^j_{BB}$ in the Fourier domain, or the mean value of the corresponding image in the spatial domain. Regularizing effects were obtained by removing the negative frequencies and by choosing an appropriate $\epsilon$.

## APPENDIX B
## FISHER INFORMATION-BASED BACKPROJECTION WEIGHTING FUNCTION DERIVATION FOR FBP OF TOF PET

In this appendix, we use the Fisher information-based method to derive the backprojection weighting function for FBP providing minimal variance in the central reconstructed pixel of a particular rotationally symmetrical phantom. Although equations (8) and (9) approximate image quality properties for converged MLEM, as explained in section II-B1, they can also be used to predict the LLIR and covariance image for a central pixel in an FBP reconstructed image under strict assumptions.

For high count cases, the Poisson noise in the measurement can be well approximated by a Gaussian distribution. Then, MLEM reconstruction is very similar to WLS reconstruction. The weights to be applied for WLS reconstruction of a central pixel in a rotationally symmetrical object are identical for each projection angle, and change very slowly with detector position if the object is sufficiently smooth. Hence, WLS reconstruction of this central pixel reduces with good approximation to unweighted least squares reconstruction. FBP is known to yield a least squares solution if angular and detector sampling are sufficiently fine. Therefore, equations (8) and (9) are expected to provide an accurate estimate of this central pixel's LLIR and covariance image in case of FBP reconstruction, taking the above restrictions into account.

In addition, for Gaussian noise WLS is known to be an unbiased estimator with minimum variance. Therefore, equation (9) will estimate the minimal variance achievable for the central pixel of a rotationally symmetrical object. To find the corresponding backprojection weighting function for FBP, we will analyze equation (8). If sufficiently fine sampling is assumed, 2D TOF PET provides complete data, meaning that the Fisher information matrix is invertible. Therefore, we can replace the pseudo-inverse with the inverse. The shift-invariance approximation is still used, but the superscripts $j$ will be dropped for ease of notation. If also the post-filtering is omitted, the following simplified version of equation (8) is obtained:

$$l^j(\Lambda) \approx [\boldsymbol{A}^{\boldsymbol{T}}\boldsymbol{C}_{\boldsymbol{Y}}^{\boldsymbol{-1}}\boldsymbol{A}]^{-1}\boldsymbol{A}^{\boldsymbol{T}}\boldsymbol{C}_{\boldsymbol{Y}}^{\boldsymbol{-1}}\boldsymbol{A}e^j \tag{B-1}$$

If we can prove that equation (B-1) is equivalent to FBP, the post-filtering to obtain a predefined target resolution will be the same for both FBP and the Fisher information-based method. For that reason, we consider the expression without post-filtering. From expression (B-1), an FBP reconstruction is derived. This is done by studying this operator only for the central pixel $j$, and then deriving the FBP operator by assuming shift-invariance. Consequently, the resulting FBP algorithm is only "optimized" for this central pixel $j$. In this procedure, $\boldsymbol{A}^{\boldsymbol{T}}\boldsymbol{C}_{\boldsymbol{Y}}^{\boldsymbol{-1}}$ will give rise to a shift-invariant backprojection, and $[\boldsymbol{A}^{\boldsymbol{T}}\boldsymbol{C}_{\boldsymbol{Y}}^{\boldsymbol{-1}}\boldsymbol{A}]^{-1}$ to the corresponding deblurring filter.

To further simplify the expressions, we consider the central pixel $j$ in a 2D Gaussian object with zero mean and standard deviation $\sigma_{obj}$, $\text{Gauss}_{2D}\{\sigma_{obj}^2\}(\vec{x})$, with

$$\text{Gauss}_{\text{iD}}\{\sigma^2\}(\vec{x}) = \frac{1}{(\sqrt{2\pi}\sigma)^i}\exp(\frac{-|\vec{x}|^2}{2\sigma^2}), \tag{B-2}$$

where $\vec{x}$ represents the $i$-dimensional location vector in the spatial domain and $|\cdot|$ denotes the vector norm.

For this derivation, we first study the operator $\boldsymbol{A}^{\boldsymbol{T}}\boldsymbol{C}_{\boldsymbol{Y}}^{\boldsymbol{-1}}\boldsymbol{A}$ by analyzing step by step what it produces when applied to image $e^j$, containing unit activity in the central pixel $j$ and zero activity elsewhere. $\boldsymbol{A}e^j$ is a TOF sinogram. It is independent of the angle, and zero everywhere except for the central line of response (LOR) at $l = 0$, where it is essentially the TOF kernel $\text{Gauss}_{1D}\{\sigma_{TOF}^2\}(\tau)$ centered around pixel $j$ and rebinned in time bins:

$$\boldsymbol{A}e^j(l,\tau,\theta) = \text{Gauss}_{\text{1D}}\{\sigma_{TOF}^2\}(\tau)\cdot\delta(l), \tag{B-3}$$

with $l$ the radial coordinate of the LOR, $\tau$ the TOF dimension, $\theta$ the projection angle, and $\delta(l)$ Dirac's delta function. $\boldsymbol{C}_{\boldsymbol{Y}}$ is the covariance matrix of the (in our case Gaussian) phantom measurement. Because the measurement noise is Poisson distributed, $\boldsymbol{C}_{\boldsymbol{Y}}$ is a diagonal matrix with the mean value of the measurement in each sinogram pixel as its diagonal elements. We only need these elements for $l = 0$, so

$$\begin{aligned}\boldsymbol{C}_{\boldsymbol{Y}}(0,\tau,\theta) &= Y(0,\tau,\theta)\\ &= \text{Gauss}_{\text{1D}}\{\sigma_{TOF}^2\}(\tau)\otimes\text{Gauss}_{\text{1D}}\{\sigma_{obj}^2\}(\tau)\\ &= \text{Gauss}_{\text{1D}}\{\sigma_{TOF}^2+\sigma_{obj}^2\}(\tau).\end{aligned} \tag{B-4}$$

Then

$$\boldsymbol{C}_{\boldsymbol{Y}}^{\boldsymbol{-1}}\boldsymbol{A}e^j(l,\tau,\theta) = \frac{\text{Gauss}_{\text{1D}}\{\sigma_{TOF}^2\}(\tau)}{\text{Gauss}_{\text{1D}}\{\sigma_{TOF}^2+\sigma_{obj}^2\}(\tau)}\cdot\delta(l) \tag{B-5}$$

$$\propto \text{Gauss}_{\text{1D}}\{\sigma_{TOF}^2(1+\frac{\sigma_{TOF}^2}{\sigma_{obj}^2})\}(\tau)\cdot\delta(l), \tag{B-6}$$

where the equal sign was dropped because a constant factor has been ignored.

Backprojection $\boldsymbol{A}^{\boldsymbol{T}}$ represents again a convolution with the TOF kernel, followed by a summation over all angles:

$$\begin{aligned}&\boldsymbol{A}^{\boldsymbol{T}}\boldsymbol{C}_{\boldsymbol{Y}}^{\boldsymbol{-1}}\boldsymbol{A}e^j(\vec{x})\\ &\propto\sum_\theta\text{Gauss}_{\text{1D}}\{\sigma_{TOF}^2(2+\frac{\sigma_{TOF}^2}{\sigma_{obj}^2})\}(\vec{x}\cdot\hat{u})\cdot\delta(\vec{x}\cdot\hat{u}^\perp)\\ &\approx\frac{1}{|\vec{x}|}\text{Gauss}_{\text{2D}}\{\sigma_{TOF}^2(2+\frac{\sigma_{TOF}^2}{\sigma_{obj}^2})\}(\vec{x}).\end{aligned} \tag{B-7}$$

with $\hat{u}$ and $\hat{u}^\perp$ the 2D unit vectors in the projection direction at angle $\theta$ and the perpendicular direction, respectively. The last expression is an approximation based on the continuous case.

Secondly, the weighted backprojection operator $\boldsymbol{A}^{\boldsymbol{T}}\boldsymbol{C}_{\boldsymbol{Y}}^{\boldsymbol{-1}}$ must be derived. From equations (B-3) and (B-7) we deduce that

$$\boldsymbol{A}^{\boldsymbol{T}}\boldsymbol{C}_{\boldsymbol{Y}}^{\boldsymbol{-1}}Q\propto\sum_\theta\text{Gauss}_{\text{1D}}\{\sigma_{TOF}^2(1+\frac{\sigma_{TOF}^2}{\sigma_{obj}^2})\}\otimes Q \tag{B-8}$$

because then equation (B-7) is satisfied for $Q = \boldsymbol{A}e^j$. Consequently, the backprojection weighting function for FBP yielding minimal variance in the central pixel of a 2D Gaussian object is a 1D Gaussian with $\sigma^2 = \sigma^2_{TOF}(1 + \sigma^2_{TOF}/\sigma^2_{obj})$. This same expression was proposed by Watson in [26], based on heuristic arguments.

This FBP weighting function is, however, not globally optimal. We can only state that with this weighting function, FBP is a very good (shift-invariant) approximation of the WLS reconstruction in the neighbourhood of the center of a Gaussian object. The approximation becomes less accurate at increasing distances from the center, because the WLS reconstruction applies for every pixel $j$ a different weighted backprojection (equal to the $j$-th row of $\boldsymbol{A}^T\ \boldsymbol{C}_{\boldsymbol{Y}}^{-1}$) and a different reconstruction filter (equal to the $j$-th row of $[\boldsymbol{A}^T\boldsymbol{C}_{\boldsymbol{Y}}^{-1}\boldsymbol{A}]^{-1}$). Moreover, any other object would yield a different backprojection weight, which in general is not identical for each projection angle.

In [26], the results of a simulation study indicated that slighty lower variance could be obtained when using a slightly narrower weighting function. This difference in outcome between the simulations and the analytical derivations might be because in the latter scatter, random coincidences and attenuation are not included.

## REFERENCES

[1] M. M. Ter-Pogossian, N. A. Mullani, D. C. Ficke, J. Markham, and D. L. Snyder, ”Photon time-of-flight-assisted positron emission tomography.” *J. Comput. Assist. Tomogr.*, vol. 5(2), pp. 227-239, 1981.

[2] T. Tomitani, ”Image reconstruction and noise evaluation in photon time-of-flight assisted positron emission tomography.” *IEEE Trans. Nucl. Sci.*, vol. 28(6), pp. 4582-4589, 1981.

[3] D. L. Snyder, ”Some noise comparisons of data-collection arrays for emission tomography-systems having time-of-flight measurements.” *IEEE Trans. Nucl. Sci.*, vol. 29(1), pp. 1029-1033, 1982.

[4] W.-H. Wong, N. A. Mullani, E. A. Philippe, R. Hartz, and K. L. Gould, ”Image improvement and design optimization of the time-of-flight PET.” *J. Nucl. Med.*, vol. 24(1), pp. 52-60, 1983.

[5] A. Mallon, P. Grangeat, and P. X. Thomas, ”Comparison between three-dimensional positron emission tomography with and without time-of-flight measurement.” *IEEE Nucl. Sci. Symp. Med. Imag. Conf. Rec.*, 1992, vol. 2, pp. 988-990.

[6] D. G. Politte, ”Image improvements in positron-emission tomography due to measuring differential time-of-flight and using maximum-likelihood estimation.” *IEEE Trans. Nucl. Sci.*, vol. 37(2), pp. 737-742, 1990.

[7] T. Yamaya, T. Obi, M. Yamaguchi, and N. Ohyama, ”High-resolution image reconstruction method for time-of-flight positron emission tomography.” *Phys. Med. Biol.*, vol. 45(11), pp. 3125-3134, 2000.

[8] J. A. Kimdon, J. Qi, and W. W. Moses, ”Effect of random and scatter fractions in variance reduction using time-of-flight information.” *IEEE Nucl. Sci. Symp. Med. Imag. Conf. Rec.*, 2003, vol. 4, pp. 2571-2573.

[9] M. Conti, B. Bendriem, M. Casey, M. Chen, F. Kehren, C. Michel, and V. Panin, ”First experimental results of time-of-flight reconstruction on an LSO PET scanner.” *Phys. Med. Biol.*, vol. 50(19), 2005.

[10] R. M. Manjeshwar, Y. Shao, and F. P. Jansen, ”Image quality improvements with time-of-flight positron emission tomography for molecular imaging.” *IEEE Internat. Conf. Acoust., Speech, and Signal Proc. Proceedings*, 2005, vol. 5, pp. v/853-v/856.

[11] R. L. Harrison, S. B. Gillispie, A. M. Alessio, P. E. Kinahan, and T. K. Lewellen, ”The effect of object size, attenuation, scatter, and random coincidences on signal to noise ratio in simulations of time-of-flight positron emission tomography.” *IEEE Nucl. Sci. Symp. Med. Imag. Conf. Rec.*, 2005, vol. 4, pp. 1900-1904.

[12] S. Surti, J. S. Karp, L. M. Popescu, M. E. Daube-Witherspoon, and M. Werner, ”Investigation of time-of-flight benefit for fully 3-D PET.” *IEEE Trans. Med. Imag.*, vol. 25(5), pp. 529-538, 2006.

[13] C.-M. Kao, D. Yun, Q. Xie, and C.-T. Chen, ”An investigation of the potential benefits in trading energy resolution for timing resolution in time-of-flight positron emission tomography.” *IEEE Nucl. Sci. Symp. Med. Imag. Conf. Rec.*, 2006, vol. 4, pp. 2564-2569.

[14] L. M. Popescu and R. M. Lewitt, ”Comparison between TOF and non-TOF PET using a scan statistic numerical observer.” *IEEE Nucl. Sci. Symp. Med. Imag. Conf. Rec.*, 2006, vol. 3, pp. 1774-1780.

[15] M. Yamamoto, D. C. Ficke, and M. M. Ter-Pogossian, ”Experimental assessment of the gain achieved by the utilization of time-of-flight information in a positron emission tomograph (Super PETT I).” *IEEE Trans. Med. Imag.*, vol. 1(3),pp. 187-192, 1982.

[16] S. Surti, A. Kuhn, M. E. Werner, A. E. Perkins, J. Kolthammer, and J. S. Karp, ”Performance of Philips Gemini TF PET/CT scanner with special consideration for its time-of-flight imaging capabilities.” *J. Nucl. Med.*, vol. 48(3), pp. 471-480, 2007.

[17] C. C. Watson, ”An evaluation of image noise variance for time-of-flight PET.” *IEEE Trans. Nucl. Sci.*, vol. 54(5), pp. 1639-1647, 2007.

[18] J. S. Karp, S. Surti, M. E. Daube-Witherspoon, and G. Muehllehner, ”Benefit of time-of-flight in PET: experimental and clinical results.” *J. Nucl. Med.*, vol. 49(3), pp. 462-470, 2008.

[19] L. Parra and H. H. Barrett, ”List-mode likelihood: EM algorithm and image quality demonstrated on 2-D PET.” *IEEE Trans. Med. Imag.*, vol. 17(2), pp. 228-235, 1998.

[20] M. E. Daube-Witherspoon, S. Surti, S. Matej, M. Werner, S. Jayanthi, and J. S. Karp, ”Influence of time-of-flight kernel accuracy in TOF-PET reconstruction.” in *IEEE Nucl. Sci. Symp. Med. Imag. Conf. Rec.*, 2006, vol. 3, pp. 1723-1727.

[21] J. A. Fessler, ”Statistical image reconstruction methods for transmission tomography.” in *Handbook of Medical Imaging*, J. M. Fitzpatrick and M. Sonka, Eds., vol. 2, pp. 1-70, SPIE Press, Bellingham, Wash, USA, 2000.

[22] J. A. Fessler and W. L. Rogers, ”Spatial resolution properties of penalized likelihood image reconstruction: space-invariant tomographs.” *IEEE Trans. Image Proc.*, vol. 5(9), pp. 1346-1358, 1996.

[23] J. Qi and R. M. Leahy, ”Resolution and noise properties of MAP reconstruction for fully 3-D PET.” *IEEE Trans. Med. Imag.*, vol. 19(5), pp. 493-506, 2000.

[24] K. Vunckx, D. Bequé, M. Defrise, and J. Nuyts, ”Single and multipinhole collimator design evaluation method for small animal SPECT.” *IEEE Trans. Med. Imag.*, vol. 27(1), pp. 36-46, 2008.

[25] J. W. Stayman and J. A. Fessler, ”Compensation for nonuniform resolution using penalized-likelihood reconstruction in space-variant imaging systems.” *IEEE Trans. Med. Imag.*, vol. 23(3), pp. 269-284, 2004.

[26] C. C. Watson, ”An improved kernel for analytical time-of-flight PET reconstruction.” *IEEE Nucl. Sci. Symp. Med. Imag. Conf. Rec.*, 2007, vol. 4, pp. 2721-2726.

[27] M. Conti, ”Effect of randoms on signal-to-noise ratio in TOF PET.” *IEEE Trans. Nucl. Sci.*, vol. 53(3), pp. 1188-1193, 2006.

[28] H. M. Hudson and R. S. Larkin, ”Accelerated image reconstruction using ordered subsets of projection data.” *IEEE Trans. Med. Imag.*, vol. 13(4), pp. 601-609, 1994.

[29] Y. Zhang-O’Connor and J. A. Fessler, ”Fast predictions of variance images for fan-beam transmission tomography with quadratic regularization.” *IEEE Trans. Med. Imag.*, vol. 26(3), pp. 335-346, 2007.

[30] K. Vunckx, L. Zhou, S. Matej, M. Defrise, and J. Nuyts, ”Fisher information-based evaluation of image quality for time-of-flight PET.” *IEEE Nucl. Sci. Symp. Med. Imag. Conf. Rec.*, 2007, vol. 6, pp. 4129 - 4136.

[31] A. J. Reader, P. J. Julyan, H. Williams, D. L. Hastings, and J. Zweit, ”EM algorithm system modeling by image-space techniques for PET reconstruction.” *IEEE Trans. Nucl. Sci.*, vol. 50(5), pp. 1392-1397, 2003.

[32] S. Vandenberghe, S. Matej, M. E. Daube-Witherspoon, M. Guerchaft, J. Verhaeghe, A. Bol, L. van Elmbt, I. Lemahieu, and J. S. Karp, ”Determining timing resolution from TOF-PET emission data.” *IEEE Nucl. Sci. Symp. Med. Imag. Conf. Rec.*, 2007, vol. 4, pp. 2727-2731.